

Excited States Calculated by Means of the Linear Muffin-Tin Orbital Method

M. Alouani¹ and J. M. Wills²

¹ IPCMS, Université Louis Pasteur, 23 Rue du Loess, 67037 Strasbourg, France

² Los Alamos National Laboratory, Los Alamos, NM 87545, USA

Abstract. The most popular electronic structure method, the linear muffin-tin orbital method (LMTO), in its full-potential (FP) and relativistic forms has been extended to calculate the spectroscopic properties of materials from first principles, i.e. optical spectra, x-ray magnetic circular dichroism (XMCD) and magneto-optical kerr effect (MOKE). The paper describes an overview of the FP-LMTO basis set and the calculation of the momentum matrix elements. Some applications concerning the computation of optical properties of semiconductors and XMCD spectra of transition metal alloys are reviewed.

1 Introduction

The density functional theory (DFT) of Hohenberg, Kohn, and Sham is the method of choice for describing the ground-state properties of materials [1]. However, in the initial derivation of the DFT, the eigenvalues are Lagrange multipliers introduced to orthogonalize the eigenvectors, which in their turn are used to compute the total energy and the charge density. In this formulation the eigenvalues have therefore no physical meaning and should not be considered as excited states. Nevertheless, the DFT in the local density approximation (LDA) or in its spin resolved local density formulation (LSDA), has been used successfully to compute the excited states, namely, optical and magneto-optical properties, x-ray absorption and magnetic dichroism spectra.

The LDA or LSDA were indeed intended to compute the ground-state properties of materials, and their use during the last two decades has produced an excellent track record in the computation of these properties for a wide variety of materials, ranging from simple metals to complex semiconductor superlattices. However, it is now believed that the DFT can do more than computing the ground state properties. This is because the Kohn–Sham equations could be viewed as deriving from a simplified quasi-particle (QP) theory where the self-energy is local and time averaged, i.e., $\Sigma(\mathbf{r}, \mathbf{r}', t) \approx V_{xc}(\mathbf{r})\delta(\mathbf{r} - \mathbf{r}')\delta(t)$, here $V_{xc}(\mathbf{r})$ is the local exchange and correlation potential as, for example, parameterized by Von Barth and Hedin [2]. Viewed in this way, the KS eigenvalues are then approximate QP energies and could be compared to experimental data. This argument is supported by quasiparticle calculations within the so called GW approximation of Hedin [3] showing that the valence QP energies of semiconductors are in good agreement with these obtained using LDA, and the conduction QP energies

differ by approximately a rigid energy shift [4,5]. In the literature this shift is often called “scissors-operator” shift [6].

In the last few years spectroscopy is becoming the standard tool for measuring excited states of materials. Its owes its impressive advances to the availability of synchrotron tunable highly polarized radiation. In particular, the measurement of optical, magneto-optical properties as well as magnetic x-ray dichroism are now becoming routine tasks for probing the structural and magnetic properties of materials. Considerable attention has been focused on transition-metal surfaces and thin films due to their novel physical properties different from that of bulk materials and due to potential industrial applications such as magneto-optical recording, sensors, or technology based on giant magneto-resistance. In this respect, theory is falling far behind experiment and it is becoming hard to give a basic interpretation of experimental data.

This paper, which is far from being a review paper about calculated excited states, tries to bridge the gap between experiment and theory by describing a rather quantitative method for computing excited states of materials. This method uses the local density approximation and the linear muffin-tin orbital (LMTO) method. In the first part of this paper we introduce the density functional theory and the local density approximation and justify the use of LDA eigenvalues as approximate excited states and relate them to quasiparticle energies. In the second part we describe the construction of the LMTO basis set within an all-electron full-potential approach [7,17] which will be used to determine the momentum matrix elements. We devote the third part to the determination of the momentum matrix elements. In the first part of the application section we present some examples of computation of semiconductors optical spectra [9,10], and leave out the optical properties of metals and magneto-optical properties of materials and refer the reader to Ref. [11,12,9,14–19]. In the second part of the applications we show some examples of x-ray magnetic dichroism calculations [20–22].

2 Density Functional Theory

The density functional method of Hohenberg and Kohn [1] which states that the ground state total energy of a system of N interacting electrons in an external potential V_{ext} is a functional of the electron density $\rho(\mathbf{r})$ does not provide an analytical form of the functional [1]. This method remains numerically intractable without the Kohn and Sham introduction of the so called local density approximation [1] in which the exchange and correlation functional $E_{xc}\{n\}$ appearing in the total energy:

$$E\{n\} = T\{n\} + \frac{e^2}{2} \int d^3r \int d^3r' \frac{n(\mathbf{r})n(\mathbf{r}')}{|\mathbf{r} - \mathbf{r}'|} + E_{xc}\{n\} \\ + \int d^3r V_{\text{ext}}(\mathbf{r})n(\mathbf{r}) + E(V_{\text{ext}}) \quad (1)$$

is given by $E_{xc}\{n\} = \int d^3r \epsilon_{xc}(n(\mathbf{r}))n(\mathbf{r})$ where ϵ_{xc} is the exchange-correlation energy of a uniform electron gas of density n . Thus, Kohn and Sham constructed a set of self-consistent single-particle equations:

$$\left(-\nabla^2 + \frac{\delta}{\delta n}(E - T)\right)\psi(\mathbf{r}) = e_i\psi_i(\mathbf{r}) \quad (2)$$

where the density $n(\mathbf{r})$ is given by:

$$n(\mathbf{r}) = \sum_i \theta(e_i < E_F) \psi_i(\mathbf{r}) \psi_i^\dagger(\mathbf{r}) \quad (3)$$

and

$$V_{\text{ext}}(\mathbf{r}) = -e^2 \sum_{R\tau} \frac{Z_\tau}{|\mathbf{r} - \tau - \mathbf{R}|} \quad (4)$$

$$E(V_{\text{ext}}) = e^2 \sum_{\tau R} \sum_{\tau' R'} (1 - \delta(R, R')\delta(\tau, \tau')) \frac{Z_\tau Z_{\tau'}}{|\tau + \mathbf{R} - \tau' - \mathbf{R}'|} \quad (5)$$

Instead of the true kinetic energy of the electron gas, Kohn and Sham used the homogeneous electron kinetic energy:

$$\bar{T} \equiv \sum_i \theta(e_i < E_F) \int d^3r \psi_i^\dagger(-\nabla^2)\psi_i \quad (6)$$

This use of homogeneous-electron kinetic energy in the Kohn-Sham equations redefined the exchange-correlation function to be:

$$\bar{E}_{xc}\{n\} \equiv (E_{xc}\{n\} + T\{n\} - \bar{T}) = \int d^3r \epsilon_{xc}(n(\mathbf{r}))n(\mathbf{r}) \quad (7)$$

It is then crucial to use a good basis-set for the description of the electronic structure of realistic systems. The augmented plane wave [23] (APW), and the Korringa-Kohn-Rostoker [24] (KKR) methods can be used, in principle, to solve exactly the Kohn-Sham equations, however these methods are numerically involved and their linearization, introduced by Andersen is much preferable. Andersen linearization, has not only made the techniques for solving the band-structure problem transparent by reducing it essentially to the diagonalization of one-electron Hamiltonian, and cuts the cost of computation by at least one order of magnitude. The linearized versions of these two powerful methods are the linear augmented plane wave (LAPW) and linear muffin-tin orbital (LMTO) methods, respectively [17].

In this paper, we will only use the LMTO method to study excited states of solids. The reason for this choice is that the LMTO method is the mostly

used method in computational electronic structure. This is due primarily to the use of atomic-sphere approximation (ASA) which made the LMTO method run fast even on today's cheap personal computers. Due to this reduced computational cost, the LMTO ASA method became the method of choice of researchers without access to supercomputers.

3 Quasiparticle Theory and Local-Density Approximation Link

The quasiparticle (QP) electronic structure of an interacting many-body system is described by the single-particle eigenstates resulting from the interaction of this single particle with the many-body electron gas of the system. The single-particle eigenstate energies are the results of solving a Schrodinger like equation containing the non-local and energy-dependent self-energy instead of the exchange-correlation potential appearing in Kohn–Sham like equations:

$$(T + V_H + V_{\text{ext}})\Psi(\mathbf{r}) + \int d^3r' \Sigma(\mathbf{r}, \mathbf{r}', E)\Psi(\mathbf{r}') = E\Psi(\mathbf{r}).$$

Thus the self-energy Σ contains all many-body effects. Almost all ab-initio QP studies were performed within the so-called *GW* approximation, where the self-energy Σ is calculated within Hedin's *GW* approximation. This method consists of approximating the self-energy as the convolution of the LDA self-consistent Green function G and the screened coulomb interaction W within the random-phase approximation. The QP eigenvalues are often obtained using first-order perturbation theory starting from LDA eigenvalues and eigenvectors [4,25]. Although there are early calculations starting from Hartree-Fock [26] or tight-binding [27] methods. Nevertheless, the best results are based on a LDA starting point [4,25,28–30].

Thus the *GW* predicted optical excitations energies of semiconductors are within 0.1 eV from the experimental results and the surprising fact is that the QP wave functions are almost identical to these produced within the LDA [4] (the wave function overlap is more than 99%). For a general review of *GW* calculations see the review by Araysetianwan and Gunnarsson [29] or by Aulbur, Jönsson and Wilkins [30].

It is clear that the quasiparticle Schrodinger equation resembles to the Kohn–Sham equation. Both equations describe a fictitious electron moving in a effective potential. The difference is that the self-energy is nonlocal and energy dependent whereas the LDA potential is local and averaged over time. This resemblance can be further pushed by noticing that the DFT can be used to obtain excitation energies. For example, the ionization energy, I , and the electron affinity, A , are difference between ground state energies:

$$I = E(N - 1) - E(N), \quad \text{and} \quad A = E(N) - E(N + 1)$$

where N is the number of electrons of the system. And since the DFT gives the correct ground state energies it should produce, in principle, the correct ionization and electron affinity energies. For metals, the addition or removal of an electron from the system costs the same energy, and hence the ionization energy is equal to the electron affinity. For insulators, the energy gap makes all the difference and hence breaks this symmetry. Thus the energy band gap is given by:

$$E_g = I - A = E(N + 1) + E(N - 1) - 2E(N)$$

In practice, however, the calculation is often obtained within the LDA and the energy band gap is calculated as the difference between the lowest conduction band and the highest valence band. It was shown by Sham and Schlüter [31] and Perdew and Levy [32] that the calculated energy gap differ from the true band gap by an amount Δ even when the DFT is used without the LDA. The Δ value could range from 50% in the case of silicon to 100% in the case of germanium. For most of the semiconductors, the GW calculations show that the LDA eigenvalues differ from the GW quasiparticle energy by a constant Δ which is almost independent of the \mathbf{k} -point. This finding is important and shows that the LDA eigenvalues have some meaning and could be used to calculate excited states. So as stated in the introduction, the Kohn–Sham equations could be viewed as deriving from a simplified quasi-particle (QP) theory where the self-energy is made local and time averaged, i.e., $\Sigma(\mathbf{r}, \mathbf{r}', t) \approx V_{xc}(\mathbf{r})\delta(\mathbf{r} - \mathbf{r}')\delta(t)$. This approximation is certainly good for metals where we have a good data base for excited state calculated within the LDA [11,12,9,14–19] and where the agreement with experiment is good. For semiconductors, this approximation is not bad either, provided we know the value of the discontinuity of the exchange and correlation. Usually, this value is provided by GW calculations or by experiment.

4 The Full-Potential LMTO Basis Set

In this section we describe the LMTO basis-set used to calculate the excited states of solids. We discuss the basis used for an all electron calculation where the potential is not supposed to be spherically symmetric nor of muffin-tin type. The use of a general potential makes the study of open structures possible without having to resort to the so-called “empty-sphere” approximation. To define the basis-set, we divide the space into non overlapping spheres called “muffin-tin” spheres and a region between these spheres which we call interstitial region. Inside the muffin-tin spheres the Schroedinger equation is solved at a fixed energy for each angular momentum ℓ and variational parameter κ (which is defined later). The linearization amounts to the use of a linear combination of the solution $\phi_\ell(e, r)$ of the Schroedinger equation for a fixed energy and its energy derivative $\dot{\phi}_\ell(e, r)$ inside the muffin-tin spheres. These linear combinations match continuously and differentiably to an envelop function (spherical function) in the interstitial region. The Bloch wave function in the interstitial region is given by a linear combination of these Hankel functions centered at each site:

$$\psi_i(\mathbf{k}, \mathbf{r}) = \sum_R e^{i\mathbf{k} \cdot \mathbf{R}} \mathcal{K}_{L_i}(\kappa_i, \mathbf{r} - \tau_i - \mathbf{R}) \quad (8)$$

where i stands for the number of the basis function quantum numbers (these numbers are $\{\tau, L, \kappa, \{e_{\ell t}\}\}$), where τ is the site number, $L = (\ell, m)$ groups the two angular quantum numbers, and $e_{\ell t}$ is the linearization energy for a particular atom type t and angular momentum number ℓ . The envelop functions are defined as $\mathcal{K}_L(\kappa, \mathbf{r}) \equiv \mathcal{K}_\ell(\kappa, r) \mathcal{Y}_L(\hat{\mathbf{r}})$.

$$\mathcal{Y}_{\ell m}(\hat{\mathbf{r}}) \equiv i^\ell Y_{\ell m}(\hat{\mathbf{r}}) \quad (9)$$

$$\mathcal{K}_\ell(\kappa, r) \equiv -\kappa^{\ell+1} \begin{cases} n_\ell(\kappa r), & \text{if } \kappa^2 > 0 \\ n_\ell(\kappa r) - i j_\ell(\kappa r), & \text{if } \kappa^2 < 0, (\kappa = i|\kappa|) \end{cases} \quad (10)$$

$$\mathcal{J}_\ell(\kappa, r) \equiv \kappa^{-\ell} j_\ell(\kappa r) \quad (11)$$

Here n_ℓ is the Neumann function and j_ℓ Bessel function for the angular momentum ℓ , and $Y_{\ell m}$ are the spherical harmonics.

To get the differentiability of the wave-function at the boundary of the muffin-tin spheres, we write the envelope function inside the muffin-tin spheres. The envelope function for a muffin-tin sphere τ' is given by:

$$\sum_R e^{i\mathbf{k} \cdot \mathbf{R}} \mathcal{K}_L(\kappa, \mathbf{r} - \tau - \mathbf{R}) \Big|_{r_{\tau'} < S_{\tau'}} \quad (12)$$

$$\begin{aligned} &= \sum_{L'} \mathcal{Y}_{L'}(\hat{\mathbf{r}}_{\tau'}) \left(\mathcal{K}_{\ell'}(\kappa, r_\tau) \delta(\tau, \tau') \delta(L, L') \right. \\ &\quad \left. + \mathcal{J}_{\ell'}(\kappa, r_\tau) B_{L', L}(\tau' - \tau, \kappa, \mathbf{k}) \right) \end{aligned} \quad (13)$$

To produce smooth basis functions we require that the basis function is differentiable at the boundary of each muffin-tin sphere, i.e., that a linear combination of ϕ and $\dot{\phi}$ matches continuously and differentiably \mathcal{K} and \mathcal{J} at the boundary of the parent sphere and other spheres, respectively. Using these matching conditions at the muffin-tin spheres, the Bloch wave function inside a muffin-tin sphere τ of the unit cell at the origin is given by [7]:

$$\psi_i(\mathbf{k}, \mathbf{r}) \Big|_{r_\tau < S_\tau} = \sum_L \mathcal{Y}_L(\mathcal{D}_\tau \hat{\mathbf{r}}_\tau) U_\ell(e_{\ell t i}, r_\tau) \Omega(\ell t, e_{\ell t i} \kappa_i) \mathcal{B}_{L, L_i}(\tau - \tau_i, \kappa_i, \mathbf{k}) \quad (14)$$

where

$$U_\ell(e, r) \equiv \begin{pmatrix} \phi_\ell(e, r) \\ \dot{\phi}_\ell(e, r) \end{pmatrix} \quad (15)$$

$$\Omega(\ell t, e\kappa) \equiv S_\tau^2 \begin{pmatrix} -W(\mathcal{K}, \dot{\phi}) & -W(\mathcal{J}, \dot{\phi}) \\ W(\mathcal{K}, \phi) & W(\mathcal{J}, \phi) \end{pmatrix} \quad (W(f, g) \equiv fg' - f'g) \quad (16)$$

$$\mathcal{B}_{L, L_i}(\tau - \tau_i, \kappa_i, \mathbf{k}) \equiv \begin{pmatrix} \delta(\tau, \tau_i) \delta(L, L_i) \\ B_{L, L_i}(\tau - \tau_i, \kappa_i, \mathbf{k}) \end{pmatrix} \quad (17)$$

To add the spin dependence to the basis-set, the Bloch wave function is multiplied by the eigenvector of the Pauli spin operator $\eta_{\pm 1}$:

$$\psi_\sigma(\mathbf{k}, \mathbf{r}) = \psi(\mathbf{k}, \mathbf{r}) \eta_\sigma$$

such that:

$$\hat{\mathbf{n}} \cdot \boldsymbol{\sigma} \eta_{\pm 1} = (\pm 1) \eta_{\pm 1}$$

where η is the quantization axis chosen in advance.

5 Dielectric function

5.1 Dynamical Dielectric Function

Here we give a review of the determination of the dielectric response of a semiconductor due to the application of an electric field. We expand the description of our published work [10] by giving more details concerning the calculation of the momentum matrix elements.

An electromagnetic field of frequency ω , and a wave vector $\mathbf{q} + \mathbf{G}$ interacting with atoms in a crystal produces a response of frequency ω and a wave vector $\mathbf{q} + \mathbf{G}'$ (\mathbf{G} and \mathbf{G}' being reciprocal lattice vectors). The microscopic field of wave vector $\mathbf{q} + \mathbf{G}'$ is produced by the umklapp processes as a result of the applied field $E_0(\mathbf{q} + \mathbf{G}, \omega)$

$$E_0(\mathbf{q} + \mathbf{G}, \omega) = \sum_{\mathbf{G}'} \epsilon_{\mathbf{G}, \mathbf{G}'}(\mathbf{q}, \omega) E(\mathbf{q} + \mathbf{G}', \omega) \quad (18)$$

where $E(\mathbf{q} + \mathbf{G}, \omega)$ is the total field producing the non-diagonal elements in the microscopic dielectric function $\epsilon_{\mathbf{G}, \mathbf{G}'}(\mathbf{q}, \omega)$. The microscopic dielectric function in the random phase approximation is given by [33]:

$$\begin{aligned} \epsilon_{\mathbf{G}, \mathbf{G}'}(\mathbf{q}, \omega) &= \delta_{\mathbf{G}, \mathbf{G}'} - \frac{8\pi e^2}{\Omega |\mathbf{q} + \mathbf{G}| |\mathbf{q} + \mathbf{G}'|} \\ &\times \sum_{\mathbf{k}, n, n'} \frac{f_{n', \mathbf{k} + \mathbf{q}} - f_{n, \mathbf{k}}}{E_{n', \mathbf{k} + \mathbf{q}} - E_{n, \mathbf{k}} - \hbar\omega + i\delta} \\ &\langle n', \mathbf{k} + \mathbf{q} | e^{i(\mathbf{q} + \mathbf{G})\mathbf{r}} | n, \mathbf{k} \rangle \langle n, \mathbf{k} | e^{-i(\mathbf{q} + \mathbf{G}')\mathbf{r}} | n', \mathbf{k} + \mathbf{q} \rangle \end{aligned} \quad (19)$$

Here n and n' are the band indexes, $f_{n,\mathbf{k}}$ is the zero temperature Fermi distribution, and Ω is the cell volume. The energies $E_{n,\mathbf{k}}$ and the crystal wave function $|n,\mathbf{k}\rangle$ are produced for each band index n and for each wave vector \mathbf{k} in the Brillouin zone.

The macroscopic dielectric function in the infinite wave length limit is given by the inversion of the microscopic dielectric function:

$$\begin{aligned}\epsilon(\omega) &= \lim_{\mathbf{q} \rightarrow \mathbf{0}} \frac{1}{[\epsilon_{\mathbf{G},\mathbf{G}'}^{-1}(\mathbf{q},\omega)]_{\mathbf{0},\mathbf{0}}} \\ &= \epsilon_{\mathbf{0},\mathbf{0}}(\omega) - \lim_{\mathbf{q} \rightarrow \mathbf{0}} \sum_{\mathbf{G},\mathbf{G}' \neq \mathbf{0}} \epsilon_{\mathbf{0},\mathbf{G}}(\mathbf{q},\omega) T_{\mathbf{G},\mathbf{G}'}^{-1}(\mathbf{q},\omega) \epsilon_{\mathbf{G}',\mathbf{0}}(\mathbf{q},\omega)\end{aligned}\quad (20)$$

where $T_{\mathbf{G},\mathbf{G}'}^{-1}$ is the inverse matrix of $T_{\mathbf{G},\mathbf{G}'}$ containing the elements $\epsilon_{\mathbf{G},\mathbf{G}'}$ with \mathbf{G} and $\mathbf{G}' \neq \mathbf{0}$. The first term of this equation is the interband contribution to the macroscopic dielectric function and the second term represent the local-field correction to ϵ . The most recent ab-initio pseudopotential calculation found that the local-field effect reduces the static dielectric function by at most 5% [6]. Previous calculations with the same method have also found a decrease of ϵ_∞ by about the same percentage [4,34]. For insulators the dipole approximation of the imaginary part of the first term of equation (21) is given by [35]:

$$\epsilon_2(\omega) = \frac{e^2}{3\omega^2\pi} \sum_{n,n'} \int d\mathbf{k} |\langle n,\mathbf{k}|\mathbf{v}|n',\mathbf{k}\rangle|^2 f_{n,\mathbf{k}}(1 - f_{n',\mathbf{k}}) \delta(e_{\mathbf{k},n',n} - \hbar\omega), \quad (21)$$

Here \mathbf{v} is the velocity operator, and in the LDA $\mathbf{v} = \mathbf{p}/m$ (\mathbf{p} being the momentum operator), and where $e_{\mathbf{k},n,n'} = E_{n',\mathbf{k}} - E_{n,\mathbf{k}}$. The matrix elements $\langle n\mathbf{k}|\mathbf{p}|n'\mathbf{k}\rangle$ are calculated for each projection $p_j = \frac{\hbar}{i}\partial_j$, $j = x$ or y and z , with the wave function $|n\mathbf{k}\rangle$ expressed in terms of the full-potential LMTO crystal wave function described by equations (14) and (8). The \mathbf{k} -space integration is performed using the tetrahedron method [36] with a large number of irreducible \mathbf{k} points the Brillouin zone. The irreducible \mathbf{k} -points are obtained from a shifted \mathbf{k} -space grid from the high symmetry planes and Γ point by a half step in each of the k_x , k_y , and k_z directions. This scheme produces highly accurate integration in the Brillouin zone by avoiding high symmetry points.

5.2 Momentum Matrix Elements

To calculate these matrix elements we first defined a tensor operator of order one out of the momentum operator $\nabla_0 = \nabla_z = \frac{\partial}{\partial z}$ and $\nabla_{\pm 1} = \mp \frac{1}{\sqrt{2}}(\frac{\partial}{\partial x} \pm i\frac{\partial}{\partial y})$. The muffin-tin part of the momentum matrix elements is calculated using the commutator $[\nabla^2, x_\mu] = 2\nabla_\mu$ so that:

$$\begin{aligned}\int_{S_\tau} d\mathbf{r} \phi_{\tau\ell'}(r) Y_{\ell'm'}(\widehat{\mathbf{r}-\boldsymbol{\tau}}) \nabla_\mu \phi_{\tau\ell}(r) Y_{\ell m}(\widehat{\mathbf{r}-\boldsymbol{\tau}}) &= -\frac{i}{2} G_{\ell m, \ell' m'}^{1\mu} \\ \int_0^{S_\tau} r^2 dr \phi_{\tau\ell'}(\frac{2}{r} \frac{d}{dr} r + \frac{\ell(\ell+1) - \ell'(\ell'+1)}{r}) \phi_{\tau\ell}(r) &\end{aligned}\quad (22)$$

where $G_{\ell m, \ell', m'}^{1\mu}$ are the usual Gaunt coefficients, and S_τ is the radius of the muffin-tin sphere of atom τ . In the interstitial region the plane-wave representation of the wave function (see equation 8) makes the calculation straightforward, but a special care has to be taken for the removal of the extra contribution in the muffin-tin spheres. However, we find it much easier and faster to transform the interstitial matrix elements as an integral over the surface of the muffin-tin spheres using the commutation relation of the momentum operator and the Hamiltonian in the interstitial region. The calculation of the interstitial momentum matrix elements is then similar to the calculation of the interstitial overlap matrix elements. The $\kappa = 0$ case has been already derived by Chen using the Korringa, Kohn and Rostoker Greens-function method [37]. We have tested that both the plane-wave summation and the surface integration provide the same results.

$$-\nabla^2 \mathbf{p}\psi = \kappa^2 \mathbf{p}\psi$$

A Hankel function can be integrated over a volume by knowing its integral over the bounding surface:

$$\begin{aligned} & \int_{\mathcal{I}} d^3r \nabla (\psi_1^\Lambda \nabla p_i \psi_2 - (\nabla \psi_1^\Lambda) p_i \psi_2) \\ &= (\kappa_1^2 - \kappa_2^2) \int_{\mathcal{I}} d^3r \psi_1^\Lambda p_i \psi_2 \end{aligned} \quad (23)$$

The surface of the interstitial consists of the exterior of the muffin-tin spheres and the unit cell boundary.

Over the surface of the muffin tins: the surface area is $S^2 d\Omega$ and the normal to the sphere points inward

$$\begin{aligned} & (\kappa_1^2 - \kappa_2^2) \int_{\mathcal{I}} d^3r \psi_1^\Lambda p_i \psi_2 = \\ & - \sum_{\tau} S_\tau^2 \int d^S \left(\psi_1^\Lambda \frac{\partial}{\partial r} p_i \psi_2 - \left(\frac{\partial}{\partial r} \psi_1^\Lambda \right) p_i \psi_2 \right) \end{aligned} \quad (24)$$

At a muffin-tin sphere boundary S_τ the Bloch wave function is given by:

$$\begin{aligned} \psi_i(\mathbf{k}, \mathbf{r}) \Big|_{S_\tau} &= \sum_R e^{i\mathbf{k} \cdot \mathbf{R}} \mathcal{K}_{L_i}(\kappa_i, \mathbf{r} - \tau_i - \mathbf{R}) \Big|_{S_\tau} \\ &= \sum_{\ell m} \mathcal{Y}_{\ell m}(\hat{\mathbf{r}}) K_\ell(\kappa_i, S) B_{\ell m, \ell_i m_i}(\tau - \tau_i, \kappa_i, \mathbf{k}) \end{aligned} \quad (25)$$

where $B_{\ell m, \ell_i m_i}(\tau - \tau_i, \kappa_i, \mathbf{k}) = \begin{pmatrix} \delta(\tau, \tau_i) \delta(\ell, \ell_i) \delta(m, m_i) \\ B_{\ell m, \ell_i m_i}(\tau - \tau_i, \kappa_i, \mathbf{k}) \end{pmatrix}$ and $K = \begin{pmatrix} \mathcal{K} \\ \mathcal{J} \end{pmatrix}$

Let W denote the Wronskian $W(f, g) = fg' - f'g$

We define then

$$S^2 W_0 = S^2 W(K_\ell^T(\kappa), K_\ell(\kappa)) = \begin{pmatrix} 0 & 1 \\ -1 & 0 \end{pmatrix}$$

and

$$\begin{aligned} w_{\tau\ell\kappa_1, \kappa_2} &= S_\tau \frac{W(K_\ell^T(\kappa), K_\ell(\kappa)) - W_0}{\kappa_1^2 - \kappa_2^2} \\ \mathbf{p}\psi_i|_\tau &= \sum_\mu \hat{\mathbf{e}}_\mu \sum_{\ell m} \left[K_{\ell-1m-\mu} \begin{pmatrix} \kappa_i^2 & 0 \\ 0 & 1 \end{pmatrix} \mathcal{G}(\ell-1, m-\mu; \ell, m; 1, \mu) \right. \\ &\quad \left. - K_{\ell+1m-\mu} \begin{pmatrix} 1 & 0 \\ 0 & \kappa_i^2 \end{pmatrix} \mathcal{G}(\ell+1, m-\mu; \ell, m; 1, \mu) \right] \\ &\quad B_{\ell m, \ell_i m_i}(\tau - \tau_i, \kappa_i, \mathbf{k}) \end{aligned} \quad (26)$$

then

$$\begin{aligned} \langle \psi_f \mathbf{p}\psi_i \rangle_\tau &= \\ &\sum_\tau \sum_\mu \hat{\mathbf{e}}_\mu \sum_{\ell m} \left[B_{\ell-1m-\mu, \ell_f m_f}(\tau - \tau_f, \kappa_f, \mathbf{k}) w_{\tau\ell-1}(\kappa_f, \kappa_i) \right. \\ &\quad \times \begin{pmatrix} \kappa_i^2 & 0 \\ 0 & 1 \end{pmatrix} \mathcal{G}(\ell-1, m-\mu; \ell, m; 1, \mu) \\ &\quad - B_{\ell+1m-\mu, \ell_f m_f}(\tau - \tau_f, \kappa_f, \mathbf{k}) w_{\tau\ell+1}(\kappa_f, \kappa_i) \\ &\quad \times \begin{pmatrix} 1 & 0 \\ 0 & \kappa_i^2 \end{pmatrix} \mathcal{G}(\ell+1, m-\mu; \ell, m; 1, \mu) \left. \right] \\ &\quad B_{\ell m, \ell_i m_i}(\tau - \tau_i, \kappa_i, \mathbf{k}) + \Delta(f, i, \kappa_i) \end{aligned} \quad (27)$$

where

$$(\kappa_f^2 - \kappa_i^2) \Delta(f, i, \kappa_i) = \sum_\mu \hat{\mathbf{e}}_\mu(\tau_i) \left[\right. \quad (28)$$

$$\begin{aligned} &+ B_{\ell_i+1m_i-\mu, \ell_f m_f}^*(\tau_i - \tau_f, \kappa_f, \mathbf{k}) \mathcal{G}(\ell_i+1, m_i-\mu; \ell_i, m_i; 1, \mu) \kappa^2 \\ &- B_{\ell_i-1m_i-\mu, \ell_f m_f}^*(\tau_i - \tau_f, \kappa_f, \mathbf{k}) \mathcal{G}(\ell_i-1, m_i-\mu; \ell_i, m_i; 1, \mu) \kappa^2 \left. \right] \\ &+ \sum_\mu \hat{\mathbf{e}}_\mu(\tau_f) \left[\right. \quad (29) \\ &+ B_{\ell_f+1m_f+\mu, \ell_i m_i}(\tau_f - \tau_i, \kappa_i, \mathbf{k}) \mathcal{G}(\ell_f, m_f; \ell_f+1, m_f+\mu; 1, \mu) \\ &- B_{\ell_f-1m_f-\mu, \ell_i m_i}(\tau_f - \tau_i, \kappa_i, \mathbf{k}) \mathcal{G}(\ell_f, m_f; \ell_f-1, m_f+\mu; 1, \mu) \kappa^2 \left. \right] \end{aligned}$$

5.3 Velocity Operator and Sum Rules

Equation (21) can not be used directly to determine the optical properties of semiconductors, when the GW approximation or the scissors operator is used to determine the electronic structure. The velocity operator should be obtained from the effective momentum operator \mathbf{p}^{eff} which is calculated using the self-energy operator, $\Sigma(\mathbf{r}, \mathbf{p})$, of the system [38]:

$$\mathbf{v} = \mathbf{p}^{\text{eff}}/m = \mathbf{p}/m + \partial\Sigma(\mathbf{r}, \mathbf{p})/\partial\mathbf{p} \quad (30)$$

GW calculations show that the quasiparticle wave function is almost equals to the LDA wave function [4,5]. Based on this assumption, it can be easily shown [38] that in the case of the scissors operator, where all the empty states are shifted rigidly by a constant energy Δ , the imaginary part of the dielectric function is a simple energy shift of the LDA dielectric function towards the high energies by an amount Δ , i.e., $\epsilon_2^{QP}(\omega) = \epsilon_2^{\text{LDA}}(\omega - \Delta/\hbar)$. The real part of the dielectric function is then obtained from the shifted ϵ_2 using Kramers-Kronig relations. The expression of ϵ_∞^{QP} is given by:

$$\epsilon_\infty^{QP} = 1 + \frac{2e^2}{3\omega^2\pi^2} \sum_{n,n'} \int d\mathbf{k} f_{n,\mathbf{k}}(1 - f_{n',\mathbf{k}}) \frac{|\langle n, \mathbf{k} | \mathbf{p} | n', \mathbf{k} \rangle|^2}{(e_{\mathbf{k},n',n} + \Delta) e_{\mathbf{k},n',n}^2}, \quad (31)$$

ϵ_∞^{QP} is very similar to $\epsilon_\infty^{\text{LDA}}$ except that one of the interband gap $e_{\mathbf{k},n',n}$ is substituted by the QP interband gap $e_{\mathbf{k},n',n} + \Delta$.

To test for the accuracy of the calculation within the LDA the f-sum rule:

$$\frac{2}{3mn_v} \sum_{\mathbf{k}} \sum_{n,n'} f_{n,\mathbf{k}}(1 - f_{n',\mathbf{k}}) \frac{|\langle n, \mathbf{k} | \mathbf{p} | n', \mathbf{k} \rangle|^2}{e_{\mathbf{k},n',n}} = 1, \quad (32)$$

where n_v is the number of valence bands, should be always checked to ensure the accuracy of the calculations.

It is easily seen that the dielectric function ϵ_2^{QP} calculated using the scissors-operator shift does not satisfy the sum rule (ω_P is the free-electron plasmon frequency):

$$\int_0^\infty \omega \epsilon_2(\omega) d\omega = \frac{\pi}{2} \omega_P^2 \quad (33)$$

because (i) ϵ_2^{LDA} satisfies this rule, and (ii) ϵ_2^{QP} is obtained by a simple shift of ϵ_2^{LDA} by the scissors-operator Δ towards higher energies. The non simultaneous satisfaction of both the f-sum rule and the integral sum rule within the scissors approximation shows the limitation of this approximation. While the scissors operator approximation describes nicely the low lying excited states, which is seen in the good determination of the static dielectric function and the low energy structures, i.e. E_1 and E_2 , in the imaginary part of the dielectric function, it seems to fail for the description of the higher excited states. This is not surprising because the higher excited states which are free electrons like are most probably

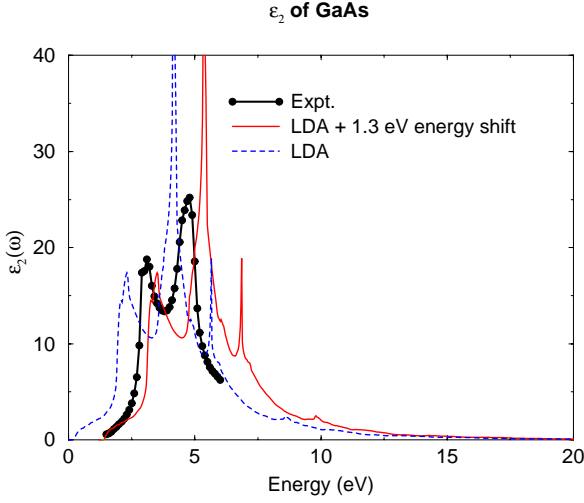


Fig. 1. Calculated Imaginary part of the dielectric function of GaAs at the experimental equilibrium volume both within LDA and shifted by 1.3 eV, compared with the experimental results of Ref. [39]. The experimental E_1 is only slightly underestimated while E_2 is overestimated. Notice that the shifted dielectric function by 1.3 eV, which produces the correct band gap, overestimates the peak positions by about 0.3 eV. Excitonic effect should shift these peaks to lower values in agreement with experiment.

well described within LDA and need no scissors-operator shift. This is supported by the fact that the the energy-loss function, $-\text{Im}\epsilon^{-1}$, within the LDA has its maximum roughly at the free electron plasmon frequency whereas within the scissors approximation its maximum is shifted to higher energies. For our purpose the scissors-operator shift remains a good approximation for the description of the low-lying excited states of semiconductors and their optical properties.

6 Applications

6.1 Optical Properties

We have used our FP-LMTO method and the formalism outlined above to calculate the optical properties of materials [9–12]. In general our results are often in good agreement with the experimental results. For semiconductors, however, good agreement with experiment is only achieved when the so called scissors-operator shift is used. Figure 1 presents our relativistic calculation of the imaginary part of the dielectric function of GaAs compared to the experimental results of Ref. [39]. The LDA relativistic results underestimate the band gap by about 1.3 eV. When the imaginary part of the dielectric function is shifted to higher energies by 1.3 eV the results the E_1 and E_2 peaks are overestimated in our calculation. One needs to shift the spectrum by less than the band gap

as done in Ref. [10] to produce good agreement with experiment. It seems then that the optical band gap is less than the band energy gap (1.5 eV). The optical band gap is produced by interband transitions to the low lying conduction states. Excitonic effects are therefore important and are responsible for the reduction of the energy gap of semiconductors. It is interesting to notice though that the static dielectric function are in good agreement with experiment for GaAs, Si, and Ge when the shift correspond to the energy band gap obtained from photoluminescence [6,10].

More interesting are the wide band-gap materials where the LDA calculated static dielectric function is in good agreement with experiment despite that the band gap is still underestimated by LDA. Correcting the band gap using the scissors operator makes the static dielectric much small than the measured value. As an example of wide gap material, we present in Figure 2 and 3 the imaginary part of the dielectric function of GaN for the cubic (3) and wurtzite structure (B4).

Table 1. Calculated static dielectric function ϵ_∞ for GaN compared to pseudopotential (PP) results and experiment. For the wurtzite structure we have calculated $\epsilon_\infty^\parallel$ for a polarization parallel to the xy plan and ϵ_∞^\perp which is perpendicular.

	zinc-blende	wurtzite	
	ϵ_∞	$\epsilon_\infty^\parallel$	ϵ_∞^\perp
PP	5.74	5.48	5.60
Present work	5.96	5.54	5.65
Expt.		5.35	5.35 ± 0.2

Table 1 shows that our LDA dielectric constant calculations are in agreement with available experimental results and the pseudo-potential (PP) results [40] including local-field effects (an error about our calculation is reported in Ref. [40]; our value for $\epsilon_\infty^\parallel$ is not 4.48 but 5.54 and the PP value should then be 4.48). It is interesting to notice that static dielectric is in good agreement for the for all the nitrides [40] while the band gap is underestimated. The scissors-operator shift fails to explain the static dielectric function of large gap semiconductor. Recently, both local-field effects and electron-hole interaction were included on an ab-initio computation of the dielectric function of few semiconductors [41,42] by extending the semi-empirical Hanke and coworkers approach [26,43] which is based on the solution of the Bethe-Salpeter equation [43]. The excitonic effects seem to improve significantly the agreement between theory and experiment. However for large band-gap semiconductors, such as diamond, the inclusion of the excitonic effects seem to underestimate the optical band gap by as much as 1 eV [42]. It is not clear from these calculations whether the static dielectric function for wide-band gap semiconductors is improved when excitonic effects are included. More theoretical work along these lines is needed to fully understand the dielectric function of wide-gap semiconductors.

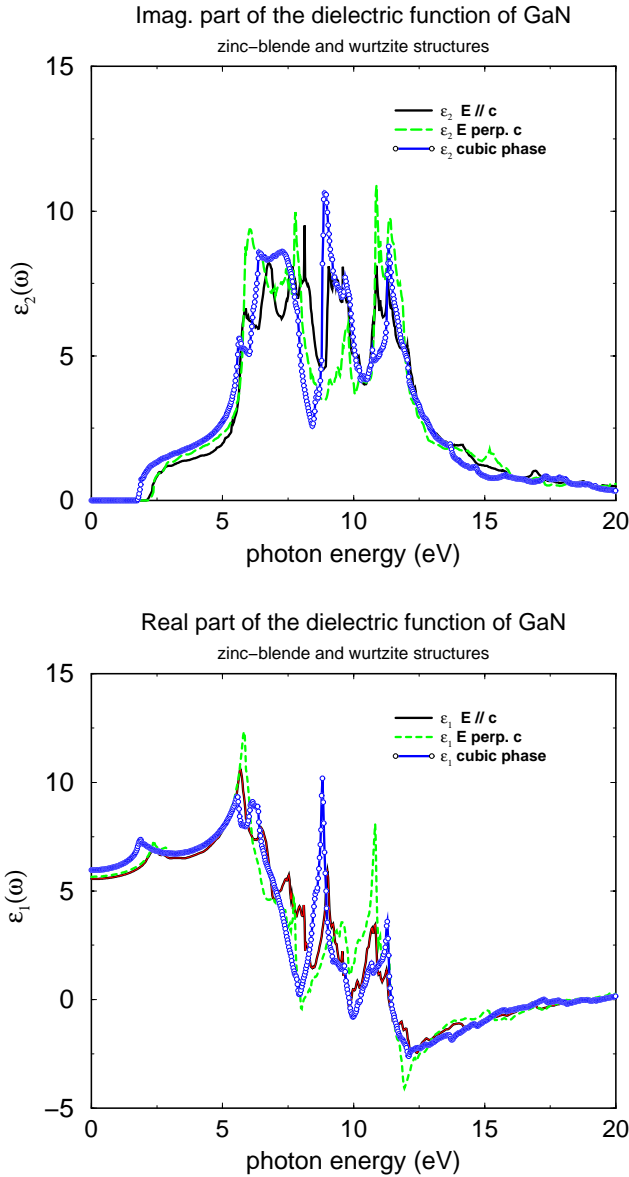


Fig. 2. Calculated imaginary and real parts of the dielectric function of GaN in its cubic and wurtzite forms. The LDA band gap of the cubic phase is 1.8 eV and the wurtzite phase is 2.2 eV.

6.2 Magnetic Circular Magnetic Dichroism

X-ray absorption spectroscopy (XAS) probes selectively each core orbital of each atomic species in a material. Two decades ago the theoretical work of Erskine

and Stern show that the x-ray absorption could be used to determine the x-ray magnetic circular dichroism (XMCD) in transition metals when left and right circularly polarized x-ray beams are used [44]. More recently these ideas were implemented experimentally and XAS was used to determine the local magnetic properties of each magnetic atomic orbital in a magnetic compound [45,46]. Thus the circular magnetic x-ray dichroism is an important tool for the investigation of magnetic materials [45–56], especially through the use of sum rules for the direct determination of the local orbital and spin contributions to the total magnetic moment [50].

Thole and co-workers show that the circular-magnetic-x-ray dichroism is related to the magnetic moment of the photo-excited atom when the core electron is excited to the conduction states that are responsible of the magnetic properties of the material. On the theoretical side, Ebert and his co-workers [51,52] have developed a fully-relativistic local-spin-density-approximation approach that was used with success to calculate the XMCD at the K-edge of Fe, the L_{3-2} -edge of Gadolinium, and Fe and Co multilayers. Wu et al used slab linear augmented plane wave method to study the $L_{2,3}$ XMCD of Fe [56]. Brouder and co-workers uses Multiple-scattering theory to solve the Schrödinger using spherical potentials and spin-orbit coupling as a perturbation in the final state [53]. Recently Ankudinov and Rehr used a method based on a non-relativistic treatment of propagation based on high order multiple scattering theory and spinor-relativistic Dirac-Fock treatment of the dipole matrix elements to calculate the Fe K edge and Gd L_3 edge XMCD [54].

The calculation of the x-ray absorption for left and right circularly polarized x-ray beams is implemented within the local-density approximation (LDA) by means of all-electron full-relativistic and spin-polarized full-potential linear muffin-tin orbital method (LMTO). The core electrons are spin-polarized and their electronic states are obtained by solving the full-Dirac equation, whereas for the valence electrons the spin-orbit coupling is added perturbatively to the the semi-relativistic Hamiltonian. The total Hamiltonian is then solved self-consistently. To calculate the polarization dependent cross-section we consider the case where the internal field polarizes the spins along the magnetization easy axis. With respect to this axis we defined the left- and right-circular polarization, which correspond to the photon helicity $(+\hbar)$ $(-\hbar)$ respectively and the following dipole interaction: $\hat{\mathbf{e}}_{\pm}\mathbf{p} = \frac{1}{\sqrt{2}}(\nabla_x \pm i\nabla_y)$. The absorption cross-section μ_{\pm} for left (+) and right (−) circular polarized x-ray calculated at the relativistic j_{\pm} ($\ell \pm \frac{1}{2}$) core level and in the dipole approximation is given by:

$$\mu_{\pm}(\omega) = \frac{2\pi}{\hbar} \sum_{m_{j\pm}} \sum_{n,\mathbf{k}} \langle j_{\pm} m_{j\pm} | \hat{\mathbf{e}}_{\pm} \mathbf{p} | n \mathbf{k} \rangle \langle n \mathbf{k} | \mathbf{p} \hat{\mathbf{e}}_{\pm} | j_{\pm} m_{j\pm} \rangle \delta(\omega - E_{n\mathbf{k}} + E_{j\pm}) \quad (34)$$

using LDA in conjunction with the relativistic full-potential LMTO technique.

Figure 3. represent the K-edge x-ray absorption of Fe, for left and right circularly polarized light, compared to the experimental results. The agreement at low energy with experiment is good and start degrading at higher energies above the mean absorption peak. It is of interest to point out that the magnetic

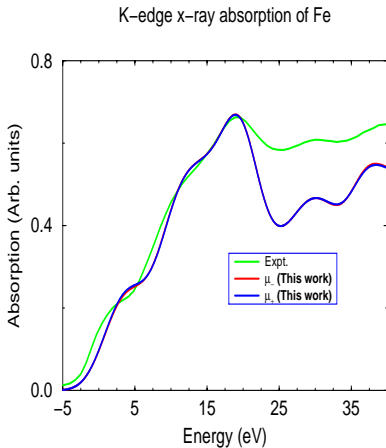


Fig. 3. Calculated x-ray absorption at the K-edge of Fe for left and right circularly polarized light compared to the experimental spectrum. The difference between the two spectra (barely visible on the graph) represents the x-ray magnetic circular dichroism.

x-ray dichroism at the K-edge which is due to the spin polarization and the spin-orbit in the final state is very small in the case of Fe. The difference between the right and left circularly polarization of the light is not even visible on the graph. However, the x-ray magnetic circular dichroism can be measured and Figure 4 shows a good agreement of the calculated dichroic signal with the experimental results of Shütz [46].

At the $L_{2,3}$ edge of $3d$ transition metals the x-ray magnetic dichroism is much important because it is mainly due to the presence of the strong spin-orbit coupling in the initial $2p$ states (in the case of Fe the spin-orbit splitting between the $2p_{3/2}$ and $2p_{1/2}$ is about 13 eV). In Figure 5 we show the calculated x-ray absorption and XMCD at the Co in PtCo ordered alloy [21].

To compare the results with experiment we have to take into account the effect of the core hole and the experimental resolution. This is done by convoluting the calculated spectra by a Lorentzian of widths of 0.9 eV and 1.4 eV for the L_2 and L_3 edges, respectively, in addition a Gaussian broadening of 0.4 eV is added to take into account the experimental resolution. The calculation of the x-ray magnetic circular dichroic signal ignoring the electron-hole recombination effect provides a semi-quantitative agreement with the experimental spectra. Hence, we believe that the core hole effect represented here by a Lorentzian broadening plays a significant role in determining the correct L_3/L_2 branching ratio for $3d$ transition metals. The underestimation of the $L_{2,3}$ branching ratio remains a challenge for theorists and further theoretical development along the line proposed by Schwitalla and Ebert [57] is needed to bring the theory at the level of the experiment.

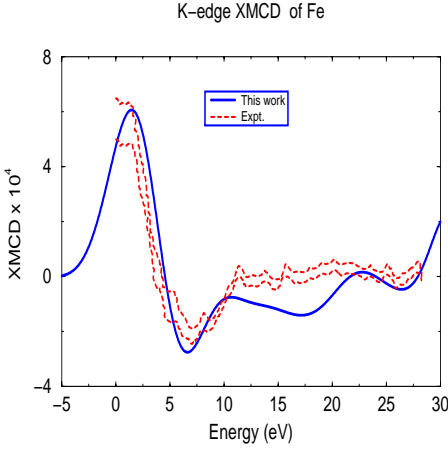


Fig. 4. Calculated x-ray magnetic x-ray dichroism at the K-edge f Fe compared to the experimental spectrum of Shütz[46].

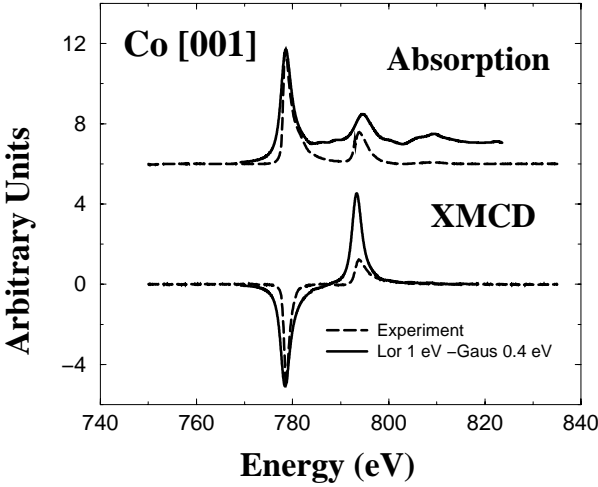


Fig. 5. Calculated x-ray absorption and magnetic x-ray dichroism at the $L_{2,3}$ -edge of Fe compared to the experimental spectrum of Grange *et al.*[21].

For the 4*d*-transition metals, the core hole is deeper, and the agreement with experiment of the XMCD is satisfactory. Figure 6 shows the calculated XMCD at the site of Pt of the CoPt ordered alloy.

In contrast to what is obtained for Co, the results for the Pt site show a much better agreement with experiment, due to the fact that the core hole effect is

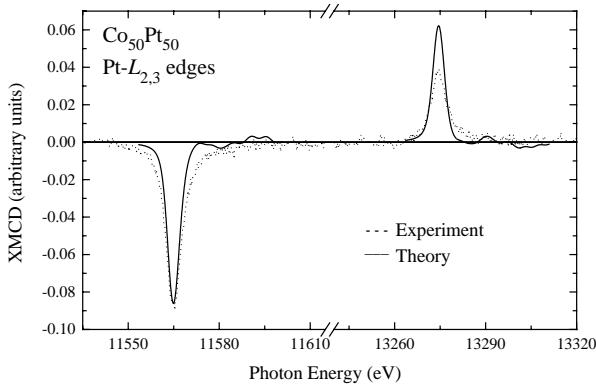


Fig. 6. Calculated x-ray magnetic x-ray dichroism at the $L_{2,3}$ -edge of Pt compared to the experimental spectrum of Grange *et al.*[21].

less intense (core hole much deeper than that of Co). For the Pt atom we used both a Lorentzian (1 eV) and a Gaussian (1 eV) to represent the core hole effect and a Gaussian of 1 eV width for the experimental resolution. The experimental and theoretical L_2 and L_3 edges are separated by a spin-orbit splitting of the $2p$ core states of 1709 and 1727 eV respectively. The width of both L_2 and L_3 edges is comparable to experiment, but the calculated L_2 edge is much larger. This produces a calculated integrated branching ratio of 1.49 which is much smaller than the experimental ratio of 2.66. Here again the theory is underestimating the branching ratio.

7 Conclusion

We have reviewed the FP-LMTO method and the implementation of the optical properties and x-ray magnetic dichroism within the local density approximation. We have showed that the momentum matrix elements can be evaluated as a muffin-tin contribution and a surface term. The method has been successfully used to compute the optical properties of metals [11,12], semiconductors [9,10] and magneto-optical properties [11] of transition metals alloys, as well as x-ray magnetic circular dichroism [20–22] with high precision.

For small-gap semiconductors a scissors-operator shift should be used to reproduce the static and dynamic dielectric function [10]. Excitonic effects seem to be important in reproducing the correct optical energy gap [41,42]. For wide-gap semiconductors the local-density approximation (LDA) static dielectric function is in good agreement with experiment and no scissors-operator shift is required despite the underestimation of the band gap by LDA [40].

For the computation of the x-ray magnetic circular dichroism the agreement with experiment is rather good [20–22,51–55]. However, the so called branching

ratio is underestimated by the theory. More theoretical work where the electron core-hole interaction is taken into account is needed to bring the theory at the quality level of experiment [57].

Part of this work was done while one of us (M.A) was at Ohio State University and were supported by NSF, grant number DMR-9520319. Supercomputer time was granted by CNUSC (project gem1917) on the IBM SP2 and by the Université Louis Pasteur de Strasbourg on the SGI O2000 supercomputer.

References

1. P. Hehenberg et W. Kohn, Phys. Rev. **136**, B864 (1964); W. Kohn et L. J. Sham, Phys. Rev. **140**, 1133 (1965).
2. U. Von Barth and L. Hedin, J. Phys. C **5**, 1629 (1972).
3. L. Hedin, Phys. Rev. **139**, A796 (1965).
4. M. S. Hybertsen and S. G. Louie, Phys. Rev. B **32**, 7005, (1985); *ibid*, **34**, 5390, (1986).
5. R. W. Godby, M. Schlüter, and L. J. Sham, Phys. Rev. B **37**, 10159 (1988).
6. Z. H. Levine and D. Allan, Phys. Rev. B **43**, 4187 (1991); Phys. Rev. Lett. **66**, 41 (1991).
7. See the article by J. M. Wills *et al.* in this book.
8. O. K. Andersen, Phys. Rev. B **12**, 3060 (1975).
9. J. Petalas, S. Logothetidis, S. Bouladakis, M. Alouani, and J. M. Wills, Phys. Rev. B **52**, 8082 (1995).
10. M. Alouani and J. M. Wills, Phys. Rev. B **54**, 2480 (1996).
11. For the calculation of magneto-optical properties of materials see A. Delin, PhD thesis, Uppsala 1998; P. Ravindran *et al.* **59** 15680 (1999).
12. R. Ahuja, S. Auluck, J. M. Wills, M. Alouani, B. Johansson, and O. Eriksson, Phys. Rev. B **55**, 4999 (1997).
13. C. S. Wang and J. Callaway, Phys. Rev. B **9**, 4897 (1979); D. G. Laurent, J. Callaway, and C. S. Wang, Phys. Rev. B **19**, 5019 (1979).
14. Yu. A. Uspenski, E. G. Maksimov, S. U. Rashkeev, and I. I. Mazin, Z. Phys. B **53**, 263 (1983).
15. M. Alouani, J. M. Koch, and M. A. Khan, J. Phys. F **16**, 473 (1986).
16. M. Amioti *et al.*, Phys. Rev. B **45**, 13285 (1992).
17. S. V. Halilov and Yu A. Uspenskii, J. Phys: Condens. Matter **2**, 6137 (1990); S. V. Halilov, *ibid* **4**, 1299 (1992).
18. P. M. Oppeneer, T. Maurer, J. Sticht, and J. Kübler, Phys. Rev. B **45**, 10924 (1992); T. Kraft, P. M. Oppeneer, V. N. Antonov, and H. Eschrig, *ibid* **52**, 3561 (1995).
19. K. W. Wierman, J. N. Hifiker, R. F. Sabiryanov, S. S. Jaswal, R. D. Kirby, J. A. Woollam, Phys. Rev. B **55**, 3093 (1997).
20. M. Alouani, J.M. Wills, and J.W. Wilkins, Phys. Rev. B **57**, 9502 (1998).
21. W. Grange, I. Galanakis, M. Alouani, M. Maret, J. P. Kappler, A. Rogalev, Phys. Rev. B (accepted).
22. I. Galanakis, S. Ostanin, M. Alouani, H. Dreyse, J. M. Wills, Phys. Rev. B (submitted).
23. J. C. Slater, **51**, 151 (1937); T. L. Loucks, *Augmented plane wave method*, (W. A. Benjamin, Inc., New York 1967)

24. J. Koringa, *Physica* **13**, 392 (1947); W. Kohn and N. Rostoker, *Phys. Rev.* **94**, 1111 (1954).
25. R. W. Godby, M. Schlüter, and L. J. Sham, *Phys. Rev. Lett.* **56**, 2415, (1986); *Phys. Rev. B* **35**, 4170, (1987); *ibid*, **36**, 6497 (1987), and **37**, 10159 (1987).
26. G. Strinati, H. J. Mattausch, and W. Hanke, *Phys. Rev. B* **25**, 2867 (1982).
27. P. A. Sterne and J. C. Inkson, *J. Phys. C* **17**, 1497 (1984).
28. M. Rohlfing, P. Krüger, and J. Pollmann, *Phys. Rev. B* **48**, 17791 (1993).
29. F. Araysetianwan and O. Gunnarsson, *Rep. Prog. Phys.* **61**, 237-312 (1998).
30. W. G. Aulbur, L. Jönsson, and J. W. Wilkins, '*Quasiparticle calculations in solids*', to be published in *Solid state Physics*; edited by H. Ehrenreich.
31. L. J. Sham and M. Schlüter, *Phys. Rev. Lett.* **51**, 1888 (1983); *Phys. Rev. B* **32**, 3883 (1985).
32. J. P. Perdew and M. Levy, *Phys. Rev. Lett.* **51**, 1884 (1983).
33. S. L. Adler, *Phys. Rev.* **126**, 413 (1962); N. Wiser, *Phys. Rev.* **129**, 62 (1963).
34. S. Baroni and R. Resta, *Phys. Rev. B* **33**, 7017 (1986).
35. H. Ehrenreich and M. L. Cohen, *Phys. Rev.* **115**, 786 (1959).
36. O. Jepsen et O. K. Andersen, *Solid State Commun.* **9**, 1763 (1971); G. Lehmann et M. Taut, *Phys. Stat. Sol.* **54**, 469 (1972).
37. A. B. Chen, *Phys. Rev. B* **14**, 2384 (1976).
38. R. Del Sole and R. Girlanda, *Phys. Rev. B* **48**, 11789 (1993).
39. D. E. Aspnes and A. A. Studna, *Phys. Rev. B* **27**, 985 (1983).
40. J. Chen, Z. H. Levine, and J. W. Wilkins, *Appl. Phys. Lett.* **66**, 1129 (1995).
41. S. Albrecht, L. Reining, R. Del Sole, and G. Onida, *Phys. Rev. Lett.* **80**, 4510 (1998).
42. L. X. Benedict, E. L. Shirley, and R. B. Bohn, *Phys. Rev. Lett.* **80**, 4514 (1998); *Phys. Rev. B* **57**, R9385 (1998).
43. G. Strinati, H. J. Mattausch, and W. Hanke, *Phys. Rev. Lett.* **45**, 290 (1980); H. J. Mattausch, W. R. Hanke, and G. Strinati, *Phys. Rev. B* **27**, 3735 (1983); N. Meskini, H. J. Mattausch, and W. Hanke, *Solid Stat. Comm.* **48**, 807 (1983); M. del Castello-Mussot and L. J. Sham, *Phys. Rev. B* **31**, 2092 (1985).
44. J. L. Erskine and E. A. Stern, *Phys. Rev. B* **12**, 5016 (1975).
45. G. van der Laan *et al.*, *Phys. Rev. B* **34**, 6529 (1986).
46. G. Shütz *et al.*, *Phys. Rev. Lett.* **58**, 737 (1987).
47. P. Carra and M. Alterelli *Phys. Rev. Lett.* **64**, 1286 (1990).
48. C. T. Chen *et al.*, *Phys. Rev. Lett.* **75**, 152 (1995) and references therein.
49. P. Carra *et al.*, *Phys. Rev. Lett.* **66**, 2595 (1991).
50. For atoms: B. T. Thole *et al.*, *Phys. Rev. Lett.* **68**, 1943 (1992), P. Carra *et al.*, *Phys. Rev. Lett.* **70**, 694 (1993), for solids: A. Ankudinov and J. J. Rehr, *Phys. Rev. B* **51**, 1282 (1995).
51. H. Ebert, P. Strange, and B. L. Gyorffy, *J. Appl. Phys.* **63**, 3055 (1988); P. Strange and B. L. Gyorffy, *Phys. Rev. B* **52**, R13091 (1995).
52. G. Y. Guo *et al.*, *Phys. Rev. B* **50**, 3861 (1994); E. Ebert, *Rep. Prog. Phys.* **59**, 1665 (1996).
53. Ch. Brouder, M. Alouani, and K. H. Bennamann, *Phys. Rev. B* **54**, 7334 (1996) and references therein.
54. A. Ankudinov and J. J. Rehr, *Phys. Rev. B* **56**, 1712 (1997).
55. N. V. Smith, C. T. Chen, F. Sette, and L. F. Mattheiss, *Phys. Rev. B* **46**, 1023 (1992).
56. R. Wu, D. Wang, and A. J. Freeman, *Phys. Rev. Lett.* **71**, 3581 (1993); R. Wu and A. J. Freeman, *Phys. Rev. Lett.* **73**, 1994 (1994).
57. J. Schwitalla and H. Ebert, *Phys. Rev. Lett.* **80**, 4586 (1998).

Magnetic Properties

